

Field-aligned current during an interval of B_Y-dominated interplanetary-field; modeled-to-observed comparisons

J. A. Carter¹, A. A. Samsonov², S. E. Milan¹, G. Branduardi-Raymont², A. J. Ridley³, L. J. Paxton⁴, B. J. Anderson⁴, C. L. Waters⁵, T. Edwards⁶

¹Department of Physics and Astronomy, University of Leicester, University Road, Leicester, LE1 7RH, UK

²Mullard Space Science Laboratory, University College London, London, UK

³1416 Climate and Space Research Building, University of Michigan, 2455 Hayward Street, Ann Arbor, Michigan 48109-2143, U.S.A.

⁴Applied Physics Laboratory, John Hopkins University, Laurel, Maryland 20723, U.S.A.

⁵The University of Newcastle Australia, Callaghan University Drive, Callaghan, NSW 2308, Australia

⁶DTU Space, National Space Institute, Centrifugevej 356 107, 2800 Kgs. Lyngby, Denmark

Key Points:

- We model an interval of interplanetary B_Y-dominated field and high solar wind densities during the impact of a CME
- The reconnection site moves rapidly from the subsolar to the high-latitude magnetopause during a rotation of interplanetary magnetic field
- Modeled and observed currents are spatially consistent in the polar cap although modeled to observed current magnitudes are often discrepant

Corresponding author: J. A. Carter, jac48@le.ac.uk

This is the author manuscript accepted for publication and has undergone full peer review but has not been through the copyediting, typesetting, pagination and proofreading process, which may lead to differences between this version and the [Version of Record](#). Please cite this article as [doi: 10.1029/2021JA029722](https://doi.org/10.1029/2021JA029722).

This article is protected by copyright. All rights reserved.

Abstract

We model an interval of remarkable interplanetary magnetic field, for which we have a comprehensive set of observational data. This interval is associated with the arrival of an interplanetary coronal mass ejection. The solar wind densities at the time are particularly high and the interplanetary magnetic field is primarily northward over many hours. This results in strong auroral emissions within the polar cap in a cusp spot, which we associate with lobe reconnection at the high-latitude magnetopause. We also observe areas of upwards field-aligned current within the summer Northern Hemisphere polar cap that exhibit large current magnitudes. The model is able to reproduce the spatial distribution of the field-aligned currents well, even under changing conditions in the incoming interplanetary magnetic field. Discrepancies exist between the modeled and observed current magnitudes. Notably, the winter Southern Hemisphere exhibits much lower current magnitudes overall. We also model a sharp transition of the location of magnetopause reconnection at the beginning of the interval, before the IMF remained northward for many hours. The reconnection location changed rapidly from a subsolar location at the low-latitude magnetopause under southward interplanetary magnetic field conditions, to a high-latitude lobe reconnection location when the field is northward. This occurs during a fast rotation of the IMF at the shock front of a magnetic cloud.

Plain Language Summary

Under extreme incoming interplanetary magnetic field conditions following the impact of an Interplanetary Coronal Mass Ejection (CME) on the Earth's system, we observe a range of phenomena in the Northern Hemisphere ionosphere. This includes auroral emissions in the form of a cusp spot and associated precipitating particles, ionospheric flows, and strong field-aligned currents in the high-latitude polar cap. These phenomena change in orientation and strength following variations in the incoming solar wind. We model the state of the magnetosphere during these observations. The modeled currents correspond well spatially with the observed currents, however the current magnitudes are very different. The modeled field-aligned currents indicate that the site of magnetic reconnection can change rapidly from a lower-latitude dayside position to a high-latitude location in the magnetospheric lobes, which is reflected in field orientation within the magnetic cloud associated with the passing CME.

1 Introduction

Phenomena observed in the ionosphere can be used to remotely sense the site of distant magnetic reconnection at the magnetopause. The ionosphere is magnetically connected to the outer magnetosphere via magnetic field lines, and hence can be used to trace how magnetic reconnection develops given incoming interplanetary magnetic field (IMF) and solar wind conditions. Southward orientated IMF results in magnetic reconnection at the lower latitude dayside magnetopause, resulting in an addition of magnetic flux to the Earth's system (Cowley & Lockwood, 1992; Dungey, 1963). However, 50% of the time the IMF will be oriented northwards, when magnetic reconnection is expected in the high-latitude magnetospheric lobes on open field lines (Sandholt et al., 1998). Northward IMF conditions do not result in an addition of flux to the Earth's system, but present a range of phenomena in the magnetosphere and ionosphere that are still under investigation including the location and extent of the reconnection site (Fear, 2021).

Distributions and magnitudes of the main field-aligned currents (FACs) region 1 and region 2 systems in the Earth's system have been related to activity at the outer magnetospheres by many authors (see Milan et al. (2017) for a review). The Region 0 current system, or under northward IMF, commonly referred to as the NBZ system, is found poleward of the region 1 current, and is often much weaker than both region 1 and region 2. In this paper, we provide an example where the NBZ current system dominates

the polar cap region and when the region 2 current is almost completely absent. NBZ currents map to high-latitude regions of the magnetosphere, poleward of the cusp, so that observations of these currents remotely sense areas of the magnetopause that experience magnetic reconnection under northward IMF conditions.

Using a magnetohydrodynamic (MHD) model, Samsonov et al. (2010) simulated the response of the ionosphere under transient conditions during the passing of an interplanetary shock, under sustained northward IMF conditions. They found the maximum NBZ to occur 2 minutes after impact of the solar wind pressure pulse at the bow shock. The region 1 FACs responded slightly later, reaching a maximum 4 to 6 minutes after impact. The NBZ FAC ionospheric footprints were shown to be static in the dayside region, and were shown to be related to a high-latitude dynamo region antisunward of the high-altitude cusps. These authors contrasted the static nature of the NBZ FAC with the more spatially variable region 1 current, whose ionospheric footprints were traced to movement from the subsolar location on the dayside along the magnetospheric flanks. In contrast Yu and Ridley (2009) simulated the ionospheric response after a moderate solar wind dynamic pressure increase under southward IMF conditions and compared this response to the northward IMF case. These authors note a fast response within 2 minutes of the ionosphere to the pressure pulse. The resulting pressure gradient in the dayside magnetosphere forms regions of vorticity that travel antisunward, leading to field-aligned currents flowing in and out of the ionosphere at dayside auroral latitudes. Neither of these studies imposed a large or varying IMF B_Y component, or explored the ionospheric response under large solar wind pressure changes.

In this work we compare a comprehensive set of observations during an event of interest, and use an MHD simulation to model the contemporaneous state of the magnetosphere. This event took place during a period of strongly northward IMF, with a varying and large IMF B_Y component, with extremely high solar wind densities. We associate this time period with a passing Interplanetary Coronal Mass Ejection (ICME) and magnetic cloud. Short incursions to southward IMF during the interval of interest prove to be significant, and we explore these in this paper. Observations during the event include auroral emissions, particle precipitations, measurements of ionospheric convection, and of FACs. The event has been characterised in Carter et al. (2020), although we provide an adapted overview of the observational evidence in this work. High-latitude magnetic reconnection in the lobes is expected during periods of northward IMF, as compared to lower-latitude magnetic reconnection on the dayside magnetopause during southward IMF, and the observations support lobe reconnection in their majority. Outputs from the MHD model include magnitudes and spatial distributions of FACs, which we use to examine the location of reconnection, and we compare these with the observations. We also use this opportunity to compare the AMPERE measured FACs with those of the MHD simulations, both spatially and in magnitude.

This paper is laid out as follows. In Section 2 we describe observations of the event of interest, using ground-based and space-based experiments, with reference to work in the literature. In Section 3 we present the MHD simulations ran for the event, including validation of these simulations using in situ measurements. We compare and discuss distributions of the field-aligned currents and the implied magnetopause boundary, between the simulations and observations in Section 4. We conclude in Section 5.

2 Observations

The observations presented in Carter et al. (2020) and summarised here included auroral emissions data obtained by the Special Sensor Ultraviolet Spectrographic Imager (SSUSI, Paxton et al. (1992); Paxton and Zhang (2016)) on board two of the Defense Meteorological Satellite Programme (DMSP) spacecraft, and supported by detections of precipitating particles by the same spacecraft. The auroral observations are ac-

122 accompanied by patterns of FACs, obtained from the Active Magnetosphere and Plane-
 123 tary Electrodynamics Response Experiment (AMPERE, Waters et al. (2020, 2001); An-
 124 derson et al. (2000)), along with ionospheric convection patterns from the Super Dual
 125 Auroral Radar Network (SuperDARN, Chisham et al. (2007)). The interval of interest
 126 spans 16 and 17 June 2012.

127 The phenomenon of particular interest here is a bright cusp spot emission feature
 128 found poleward of the main auroral oval. This cusp spot is shown in a series of images
 129 of auroral emissions and ionospheric flows in Fig. 1, which are ordered by time per row,
 130 which increases from top to bottom. The emission is observed in the Lyman Birge Hop-
 131 field (LBH) band from DMSP/SSUSI, primarily from electron-induced emission. Fur-
 132 ther images showing emission in the Lyman- α band, resulting from proton precipitation,
 133 can be found in Carter et al. (2020). LBH-long band images are shown in the left-hand
 134 column on a magnetic local time (MLT) and magnetic latitude grid with noon to the top.
 135 The cusp spot is observed to move in response to the changing IMF B_Y -component un-
 136 der a strongly northward IMF. We also plot contours of the distributions of FAC cur-
 137 rent densities in the polar cap over each auroral emissions image, at intervals of $0.5 \mu\text{A m}^{-2}$,
 138 with red and blue representing upwards and downwards FACs respectively. Accompa-
 139 nying SuperDARN-derived ionospheric flow data are shown in the right-hand column,
 140 taken at the 2-minute time step at the midway point of each DMSP satellite pass, along
 141 with derived electrostatic potential patterns and Heppner-Maynard (Heppner & May-
 142 nard, 1987) boundaries. The assumptions made in constructing the SuperDARN data
 143 products are detailed in Carter et al. (2020). The SuperDARN panels in Fig. 1, in par-
 144 ticular the first and last two right-hand column panels, show that fast flows are associ-
 145 ated with the eastern edge of the cusp spot auroral emissions, which is also the region
 146 of the channel between the NBZ FAC cells. This remains true as the auroral cusp spot
 147 swings into the dusk sector under the influence of large IMF B_Y (see below).

148 Fig. 2 panels (a) - (c) shows the IMF and solar wind conditions, as taken from OMNI
 149 data (King & Papitashvili, 2005), that spans 16 to 17 June 2012. Panels (d)-(g) contains
 150 observed and MHD-simulated geomagnetic indices, MHD and Shue et al. (1998) model
 151 derived magnetopause subsolar positions, and SuperDARN-derived cross polar cap po-
 152 tentials. The IMF is predominately northwards throughout most of the interval, although
 153 B_Y and B_Z rotate so that when B_Y is large and positive, B_Z is small and near zero or
 154 negative and vice versa. The interval terminates with a southward IMF turning at around
 155 05:00 UT. The IMF and solar wind parameters of panels (a) - (c) indicate that this in-
 156 terval included a magnetic cloud, embedded within a passing ICME. Some activity is seen
 157 in the auroral electrojet indices of AL and AU, particularly after 03:00 UT. At this time
 158 the simulated AL and AU indices diverge from the observations. The positive measured
 159 Dst index indicates significant solar wind ram pressure at the dayside magnetopause. The
 160 simulated Dst underestimates the measured values, but both measured and simulated
 161 values are positive immediately after the density pulse between 22 UT and 23 UT. The
 162 remaining panels (f) and (g) will be discussed with respect to the MHD simulations of
 163 the interval later in the text.

164 3 Magnetohydrodynamic Simulations

165 The OMNI-derived IMF and solar wind conditions before and during the interval,
 166 and described above in the observations, provided the boundary conditions for the MHD
 167 simulations. The simulations were started at 18 hr UT, giving sufficient time to initialise
 168 the system and compare the current systems from after 21 hr UT, which we discuss in
 169 the remainder of this paper. Simulations were run using the Space Weather Modeling
 170 Framework (SWMF, Tth et al. (2005)) version 20180525 provided via the Community
 171 Coordinated Modeling Center (CCMC) at 5-minute resolution. This code employs the
 172 Comprehensive Inner Magnetosphere Ionosphere model (Fok et al., 2014) to link the iono-

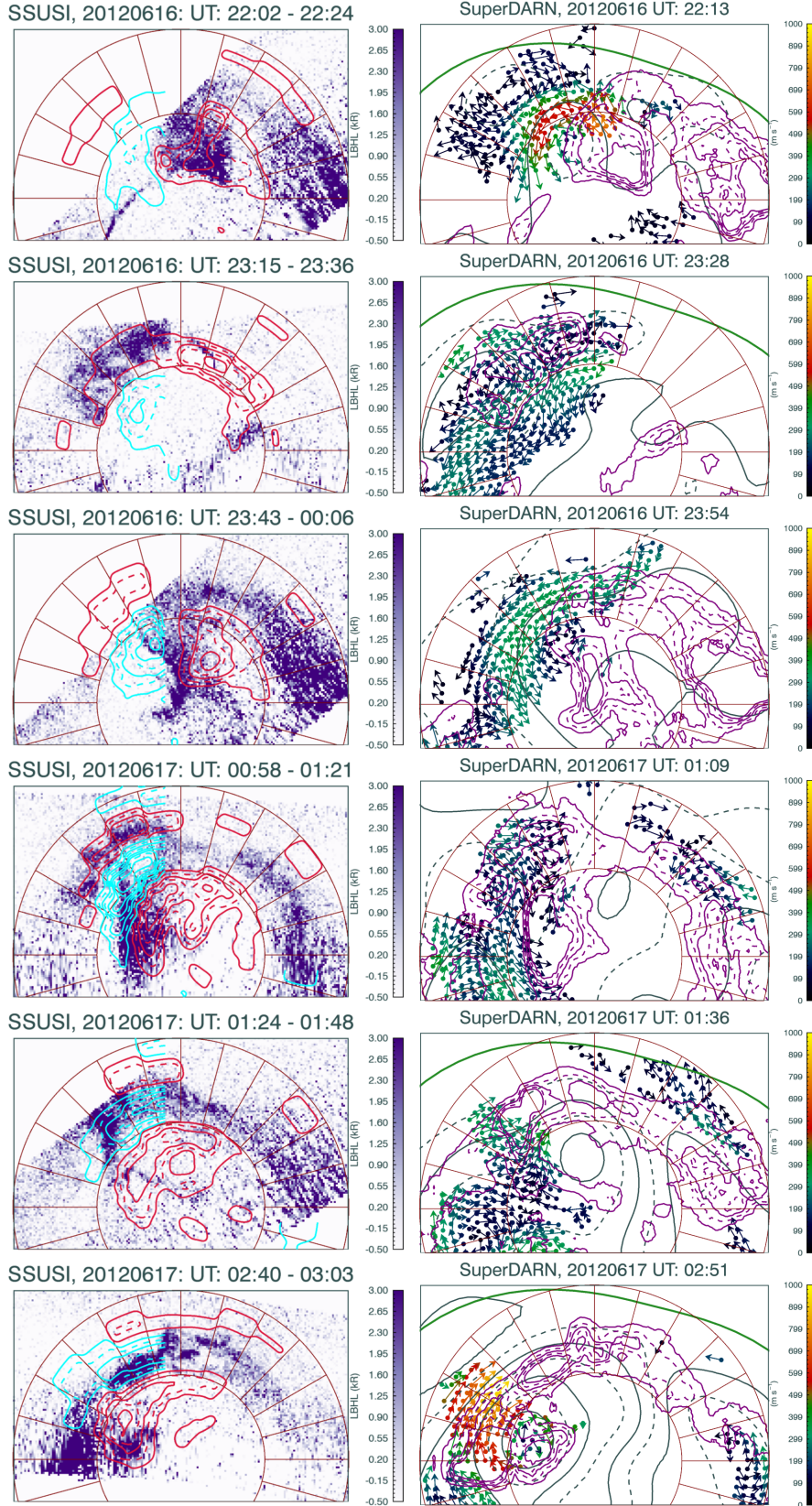


Figure 1. A sequence of images on a MLT, magnetic-latitude grid that is ordered in rows where time increases from top to bottom. Left column: DMSP/SSUSI LBH-long band images with overlaid contours of AMPERE-derived FACs, with red and blue lines for upwards and downwards currents respectively, at intervals of $0.5 \mu\text{A m}^{-2}$ magnitude. Right column: SuperDARN-derived ionosphere flows at the mid-time of each DMSP high-latitude pass of the accompanying left column, with overlaid contours of the auroral LBH-long emissions in purple. The electrostatic potential pattern contours are in gray, and the Heppner-Maynard Boundary is in green. Noon and dusk are to the top and left of each panel, respectively, while co-latitude intervals of 10° are marked in red.

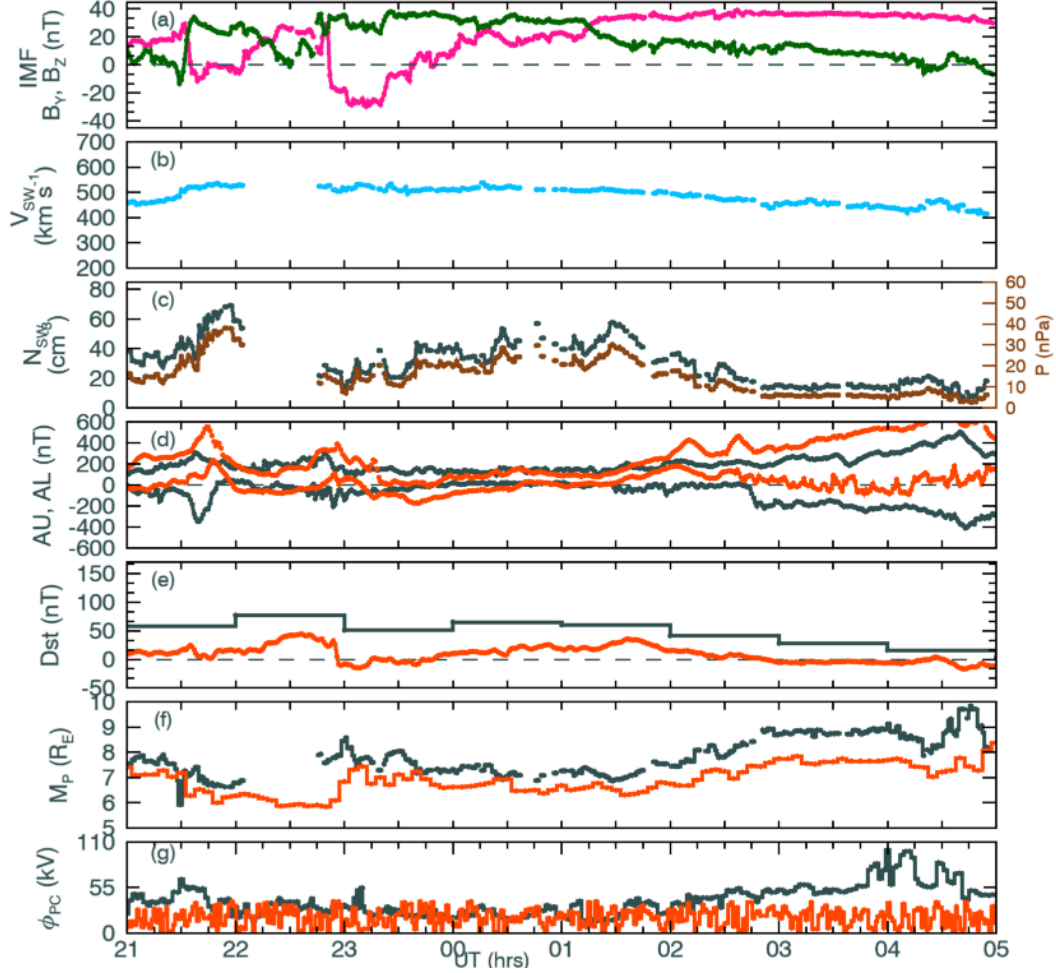


Figure 2. IMF and solar wind conditions during an interval spanning the dates 16 to 17 June 2020, with times in UT (hrs), plus MHD-simulated parameters. This figure is adapted from Carter et al. (2020). In panels (a) IMF components are shown: IMF- B_Y (pink) and B_Z (green). In (b); solar wind speed (blue). In (c); solar wind, in the upper and lower traces respectively. In (d) observed (gray) and MHD-simulated (orange) AL and AU indices. In (e); Measured (gray) and simulated (orange) Dst indices. In (f); the (Shue et al., 1998) modeled magnetopause location (gray) and the MHD modeled last-closed field line subsolar point (orange). In (g); SuperDARN-derived (gray) and the MHD-derived (orange) cross polar cap potential.

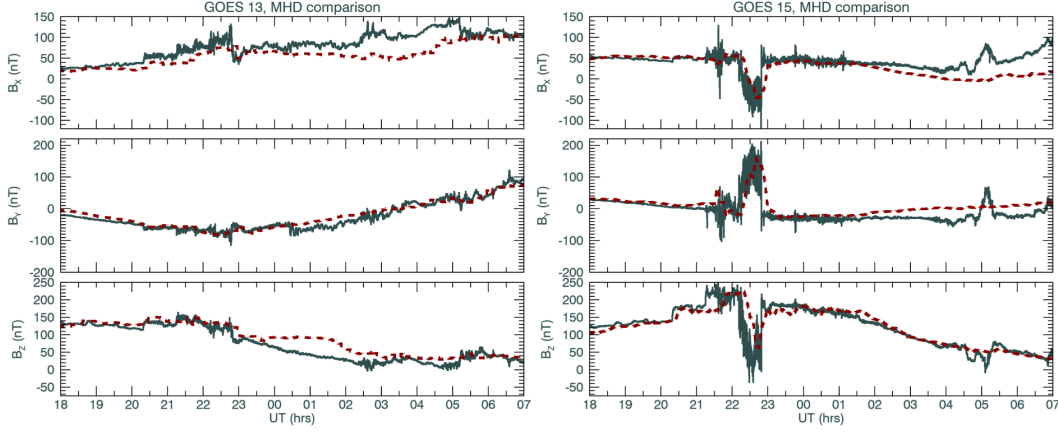


Figure 3. In situ measurements of magnetic field components, as obtained by the GOES-13 (left panel) and GOES-15 (panel) satellites in gray, with MHD simulated values in red, taken from the simulations at the orbital positions of each satellite.

sphere to the magnetosphere, and models the ring current and radiation belts, with an ionospheric electrodynamics model described by Ridley et al. (2004).

Fig. 2 panel (f) shows the subsolar point of the last closed field line of the MHD simulation (orange), and the Shue and Song (2002) model derived magnetopause subsolar position (gray). The values track each other throughout the interval, although the MHD model shows values that are earthward of the (Shue & Song, 2002) model by approximately 1 R_E . The cross-polar cap potential, in panel (g) shows smaller values for the MHD simulations than for the SuperDARN-derived values. The greatest discrepancies in the cross-polar cap potential occur at the same time as increased auroral activity as shown in the AL index of panel (d). This underprediction by the MHD model has been seen in comparisons of MHD simulations with climatological models (Gordeev et al., 2015).

To further verify the MHD simulations, in Fig. 3, we compare geocentric solar magnetospheric system (GSM) magnetic field components from the MHD simulations to in situ data obtained by the GOES-13 and GOES-15 satellites over our interval of interest, at locations in the simulations corresponding to the orbital positions of the individual satellites. These show good agreement for both satellites across all three magnetic field components throughout the interval. Although the GOES satellites are in geosynchronous orbit and are therefore not in the lobes where reconnection is expected to be taking place under northward IMF, these were the only in situ satellites with data available at the time of our interval. They do provide a means to check the MHD simulations generally (Ridley et al., 2016), and given the strong compression of the magnetosphere during this interval, a geosynchronous orbit is not far from the subsolar location of the magnetopause.

From the MHD simulation results, in Fig. 4 we plot a series of images of absolute current density and the product $E \cdot J$, in the YZ and XZ planes respectively. These are plotted at a selection of increasing times from left to right, at a distance of 4 R_E and 7 R_E from Earth for the current density plots (top two rows), and in the $Y=0$ plane for the $E \cdot J$ plots (bottom row). In the top two rows, the main magnetopause current is seen as the inner circle in each panel and the bow shock as the outer circle. Note that the colour bar changes between rows. The clock angle is negative at the beginning of the sequence at 21:30 UT, but becomes positive from 21:35 UT onwards. The southward turning of

the IMF, also shown in the IMF B_z component trace of Fig. 2 is brief. This short sub-interval is coincident with the maximum compression of the magnetopause, as estimated by the Shue et al. (1998) model magnetopause subsolar position, shown in Fig. 2f. At 21:30 UT the current density is highest in the subsolar region at $X=7 R_E$. By 21:50 UT, an enhancement is visible in the current densities at a high-latitude location, at a closer distance of $X = 4 R_E$. In the third row of Fig. 4 we plot the term $E \cdot J$ in the XZ plane, which has been calculated from the MHD simulations and represents the rate of electromagnetic-to-mechanical energy conversion. We identify the magnetic reconnection region through areas of positive $E \cdot J$, which indicates a load whereby electromagnetic energy is converted into kinetic energy (Siscoe et al., 2000; Samsonov et al., 2010). Conversely, negative values indicate where kinetic energy is converted into electromagnetic energy (purple regions), which here indicate the bow shock (white to purple areas, at a subsolar distance of approximately $9 R_E$ at 21:30 UT). At 21:30 UT the load on the magnetopause does not appear large, but increases throughout the sequence. A slightly enhanced load is seen in the northern hemisphere cusp by 21:40, when the IMF is now northward. The largest load is seen later at 21:50 UT, in the northern high-latitude cusp. These enhancements in current density and increased load are suggestive of the location of magnetic reconnection. These simulations show that this magnetic reconnection location changes rapidly between a low-latitude equatorial, subsolar location, to a high-latitude lobe location, as the IMF transitions from a southward to northward orientation.

4 Results and Discussion

In Figs. 5 and 6, we plot selected images of the AMPERE measured FACs, plotted on a 1 hour MLT and 1 degree co-latitude grid for the Northern and then the Southern Hemisphere, where Noon is towards the top of each panel. On each AMPERE image, we overplot contours of the currents estimated from the MHD simulation, and on each MHD image we plot currents of the AMPERE-observed FACs. The IMF clock angle is shown in a dial to the top right of each panel. For the Northern Hemisphere as shown in Fig. 5, the observed FACs are dominated by the area of upwards NBZ FAC at high latitudes. The region 1 and region 2 FACs, equatorward of the polar cap are much weaker than these NBZ FACs. Initially the NBZ FAC is found around the noon sector. From 01:00 UT, these NBZ FACs move across the polar cap to the dusk side, as the IMF changes direction to become increasingly B_y -dominated by the end of the interval.

In Fig. 5 for the Northern Hemisphere, we note reasonable spatial agreement between the simulated and observed currents throughout the interval. The simulation models a large upwards NBZ FAC at high latitudes that is spread over many hours of MLT, similar to the NBZ FACs observed by AMPERE. The peak current densities of the simulated upwards FACs are found within 1 to 2 hours of MLT of the observed current density peaks at UTs of 22:05 to 00:05, and 02:00 to 04:00. The difference in co-latitude between the simulated and observed peak upwards FACs is a couple of degrees. An exception occurs at 01:00 where the peak modeled current is found prior to noon and almost at the pole, whereas the observed upwards NBZ current is found spread over several MLT sectors at co-latitudes of less than 10° . Note that at this time the IMF B_y component increases, and by 02 hrs UT the IMF B_y component is greater than the IMF B_z component. For the Southern Hemisphere in Fig. 6, the current systems are much weaker overall. There is no high-latitude NBZ observed or simulated in any of the panels. At a UT of 22:05 the peak upwards observed FAC is co-located with that of the simulations in the pre-noon sector. From 02:00 to 04:00, the simulated and observed downwards FACs about Noon are co-located. (Lu et al., 2011) also reported large NBZ FAC cells in the very high-latitude polar cap, which were simulated for a period of sustained northward IMF, and were shown to be similar to those here in Fig. 5. They also found evidence of two-cell convection during this period. We do not see evidence of two-cell convection in the SuperDARN ionospheric flows in Fig. 1, however we have limited dayside coverage

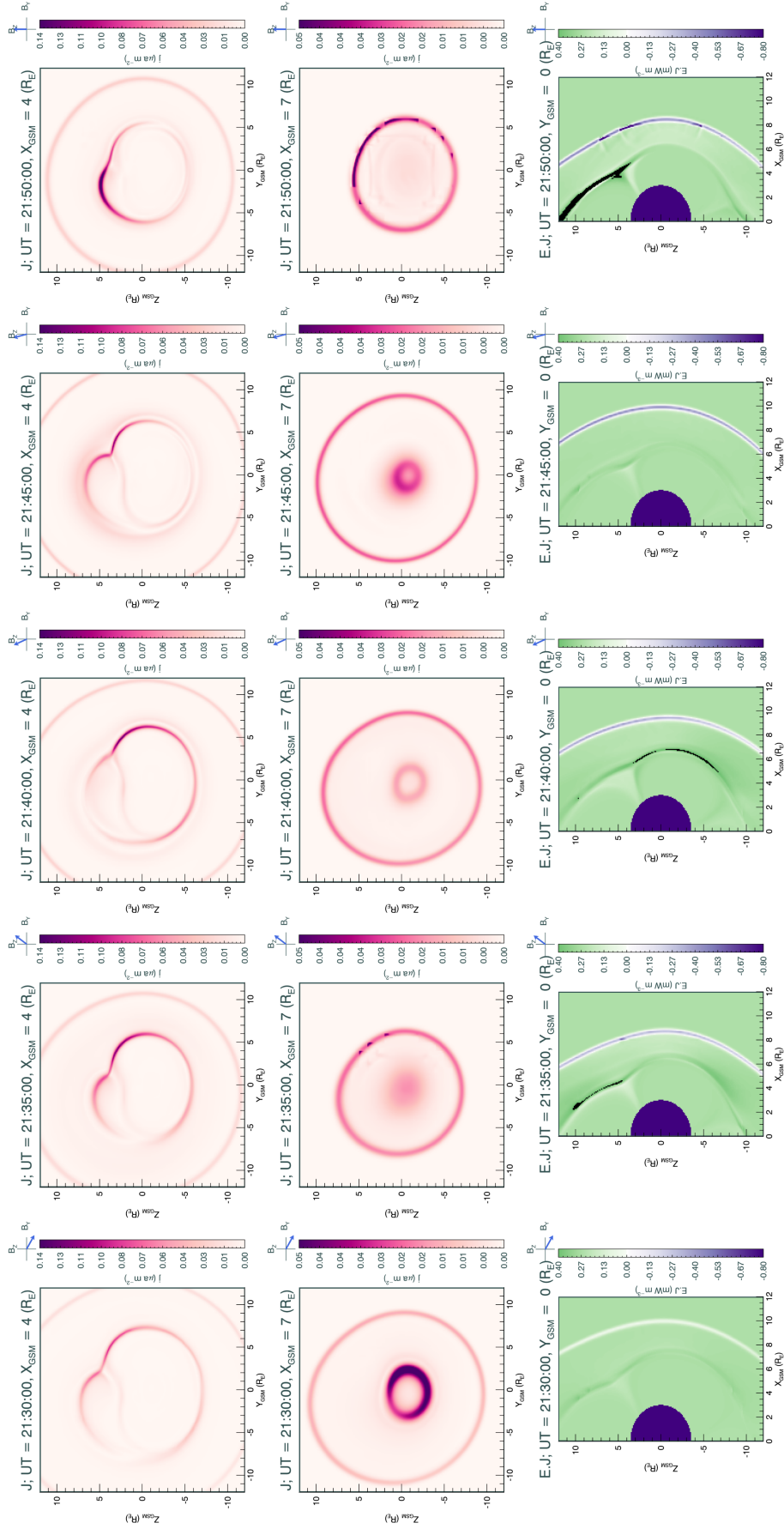


Figure 4. Images of current density and $E.J.$, from the MHD simulations at a selection of times that show a sharp transition in the IMF conditions. The upper two rows show the current density in the YZ plane at either $X=4 R_E$ or $X=7 R_E$. The bottom row shows $E.J.$ calculated at $Y=0 R_E$. Each panel includes a dial in the upper right-hand corner showing the IMF clock angle.

by the radars. During the (Lu et al., 2011) case, the IMF- B_Y component was smaller than the values we present here, with clock angles sustained near zero for several hours. The clock angle and auroral emissions from horse-collar shaped aurora presented in Lu et al. (2011) suggested that in their case, dual-lobe reconnection had occurred in the high-latitude regions of both hemispheres. In contrast to Lu et al. (2011), we only see large and high-latitude NBZ FACs in the Northern Hemisphere, and we conclude that here instead single lobe reconnection has occurred at the high-latitude magnetopause.

We explore the differences in current magnitudes between the simulations and observed FACs further below. The Southern Hemisphere is near winter solstice during this interval. In contrast, the Northern Hemisphere is approximately at summer solstice and is therefore well lit, and so will undergo increased conductivity from photoionization allowing more current to flow (Ridley et al., 2004).

In Fig. 7 we plot timeseries of the magnitude of the FACs in the high-latitude polar caps for the observed and modeled values. Currents that are located poleward of a magnetic co-latitude of 30 degrees are integrated in order to incorporate the main region 1, region 2, and NBZ polar cap current systems. We have experimented with using other co-latitude thresholds for the results shown below, which are not shown here. The same conclusions apply for larger co-latitude thresholds, whereas if we take a smaller value we see issues associated with excluding partial current systems at lower latitudes which will misinform our results. Only observed current densities that exceed a magnitude threshold of $0.2 \mu A m^{-2}$ are included, so that we minimise the effects of including weak current artefacts that result from the AMPERE data processing technique. Note that this threshold was not applied to the modelled currents. To convert from current densities into currents we assumed an altitude of 110 km to calculate the grid areas of the modelled data set, and 780 km for the AMPERE data set.

We plot the modeled and observed currents for the Northern (panels a, b, and c) and Southern (panels d, e, f) hemispheres respectively. Upwards and downwards currents are plotted in red and blue. In panels (a) and (d) we plot the current magnitudes time series. Modeled currents are shown with a solid line, and observed currents with a dashed line. In panels (b) and (e) we plot the difference between the modeled and observed currents, so that a positive value here indicates that a current magnitude has been overestimated by the model. In panels (c) and (f) we plot the mean current densities across the polar cap.

The magnitudes of the Northern Hemisphere currents in panels (a) are high, up to a maximum of approximately 8 MA near the end of the interval. The magnitudes are comparable to average current magnitudes observed during periods of high levels of auroral activity, as seen in Fig. 5 of Coxon et al. (2014). We have not split the currents into region 1, region 2, and NBZ contributions here, although from Fig. 5 we know that the NBZ FACs dominate throughout the interval. Therefore we surmise that the NBZ currents exhibit magnitudes more typical of strong region 1 and region 2 in this interval. We see that the MHD simulations underestimates the Northern Hemisphere upwards and downwards FAC magnitudes during most of the period between approximately 22 hours UT until $\sim 01:30$ UT, by up to 2 MA, in panel (a). This is also shown in the difference between modeled and observed currents in panel (b). Prior to 01:30 UT the model to observed difference fluctuated over short intervals, but tended to overestimate the currents. The interlude of underestimating the observed current corresponds to the period of peak solar wind density as shown in panel (b) of Fig. 2) and peak auroral emissions and large NBZ current cells as seen in the SSUSI images with AMPERE contours shown in Fig. 1. It is also when the IMF B_Y component is briefly negative. From 01:30 hrs UT to the end of the interval the model overestimates the observed FACs for both downwards and upwards currents, but slightly more so for the upwards currents. During this time the solar wind density drops to around 20 cm^{-3} , but the system as a whole remains active as indicated by the large bays in the AU and AL indices in panel (c) of Fig. 2. The

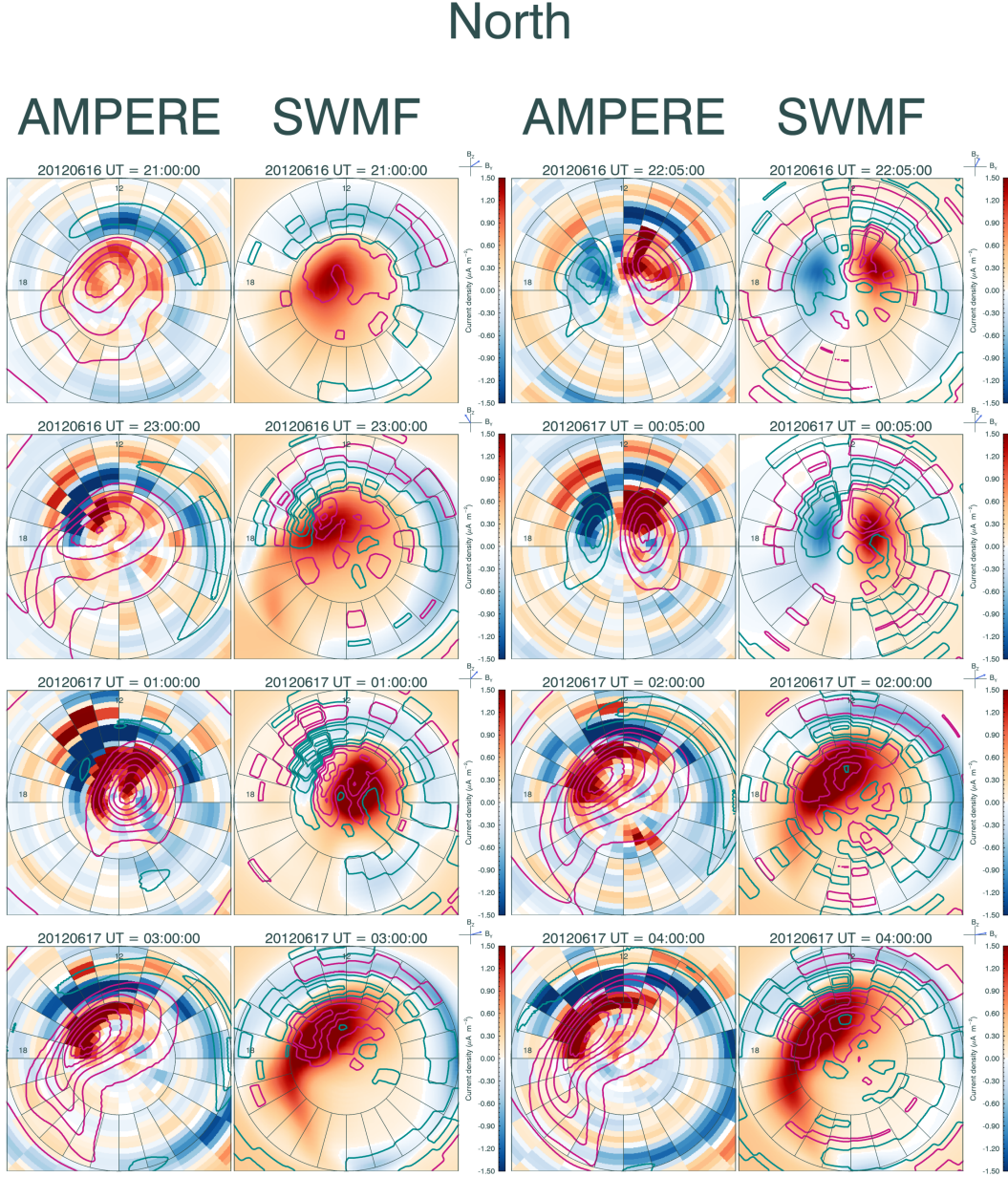


Figure 5. A series of images showing the Northern Hemisphere AMPERE-observed FACs (left-hand panels) and MHD-derived currents (right-hand panels) at select times throughout the interval. The AMPERE-observed FACs are overlaid with MHD-current contours, and the MHD-derived currents are overlaid with AMPERE-observed FAC contours. Red and blue lines depict up and down currents respectively. Contours are plotted at $0.3 \mu\text{A m}^{-2}$ current density intervals.

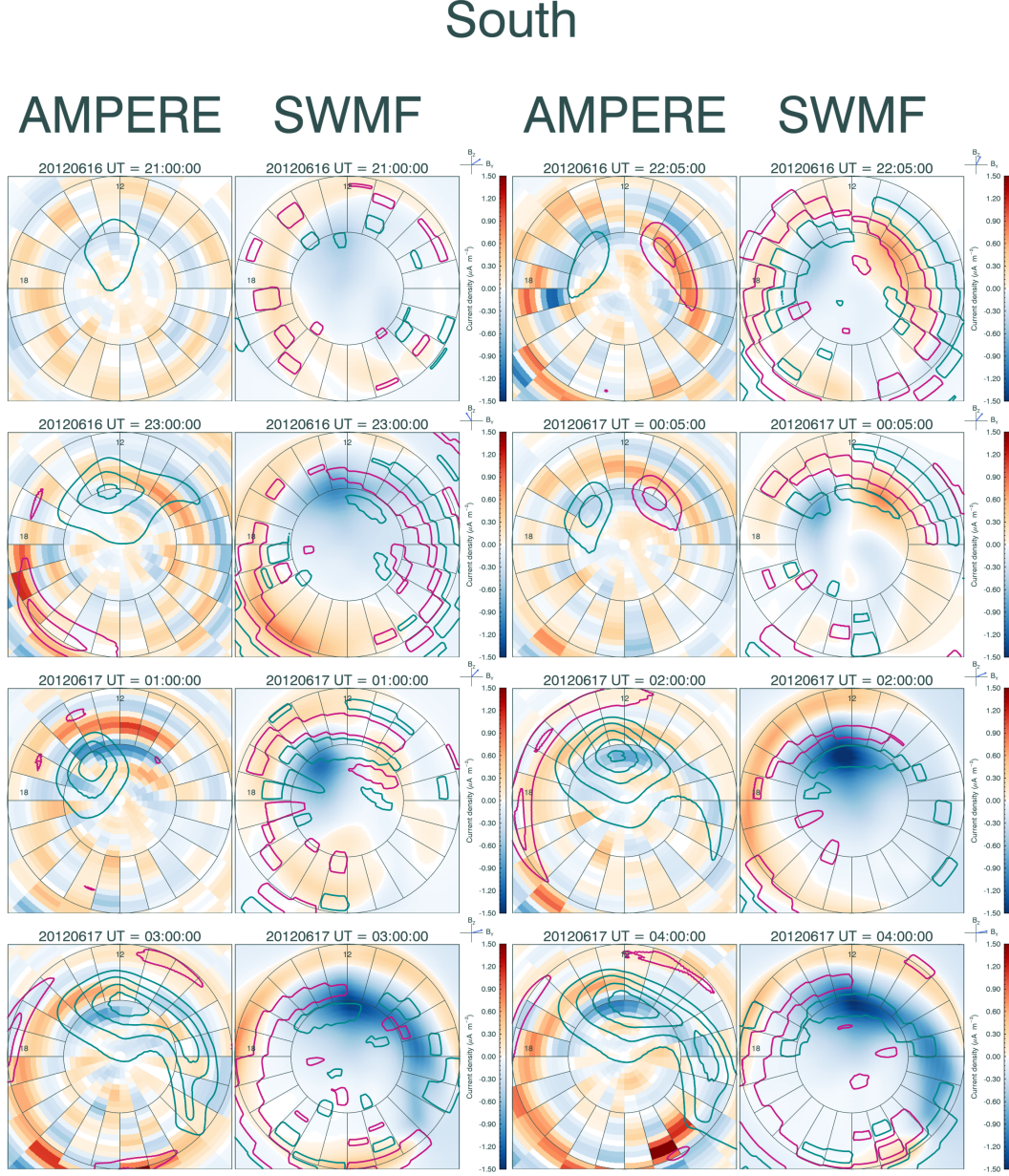


Figure 6. A series of images showing the Southern Hemisphere AMPERE-observed FACs (left-hand panels) and MHD-derived currents (right-hand panels) at select times throughout the interval. The plots are in the same format as Fig. 5.

maximum observed current density is seen at the middle of the interval about 0 UT as seen in panel (c). The modeled mean current densities show more variation than the observed values. The downwards current density mean values are considerably larger for the observed as compared to the modeled values, apart from between 23 and 0 UT when they briefly match in magnitude.

For the Southern Hemisphere, in panels (d) and (f), we observe and model much smaller current magnitudes and current densities, compared to the Northern Hemisphere. In panel (e) we see that the modeled values are less different to the observed values as compared to the discrepancies seen previously for the Northern Hemisphere. The difference between the modeled and observed values for the downwards and upwards currents track each other throughout the interval. The largest model to observation discrepancy occurs, as it does for the north, after 01:30 UT. However, throughout the entire interval, the model mainly overestimates the observed currents. This is not seen in the mean current densities of (f), where the mean observed current densities are larger than those of the model. This can be explained by considering the differences in the spatial distribution of the currents, as shown in Fig. 6. If the region 2 currents at lower latitudes are overestimated by the model then they will contribute to a greater extent to the total current given the increased area of each grid latitude-longitude grid cell with increasing co-latitude.

In panels (g) and (h) we examine the raw magnetic vectors of AMPERE, as compared to in situ measurements taken by an individual DMSP satellite along its orbital track, to test whether the AMPERE data were spurious. For this we use an example high-latitude pass of the DMSP satellite to define a time period on 16 June 2012, between UT of 23:15 and 23:36. In (g) we plot the satellite tracks of the various individual satellites that crossed the Northern Hemisphere polar cap in the morning sector of the polar cap. We show the DMSP F16 satellite track and magnetic field perturbation vectors in orange. We plot colored raw perturbation vectors for the multiple individual satellite passes that make up the AMPERE data set. All vectors are scaled in length to a reference vector. We observe that the AMPERE data set has good coverage of the high-latitude day-side sector, particularly at high latitudes slightly before noon. High numbers of measured dB vectors by numerous high-latitude passes of the the Iridium® satellites that contribute to the AMPERE data set lead to a high level of confidence in the AMPERE FAC maps. The AMPERE and DMSP vectors are of the same order of magnitude and direction in the region of strongest perturbations, approximately between 09 and 11 hr MLT. In (h) we compare a histogram of these raw perturbation vectors, where the vectors are taken from a high-latitude dayside sector from 09 hr to 11 MLT with co-latitudes of between 7 and 13 degrees. The histograms are normalised to the total number of vectors for either the DMSP satellite (orange), or the total number of contributing AMPERE vectors (blue). We see that in this limited temporal and spatial segment, the distribution of perturbation magnitudes are similar, although the DMSP data shows a small fraction of vectors with larger absolute magnitudes. The other DMSP high-latitude passes, not shown, also showed similar magnetic field perturbations between DMSP and AMPERE.

In Fig. 8 we briefly examine the AMPERE FAC maximum and mean current densities with those of the Edwards et al. (2020) empirical model within 30 degrees co-latitude in the Northern Hemisphere. The Edwards et al. (2020) model was constructed using a combination of multiple-satellite data, excluding the AMPERE data set. It is hemisphere, solar wind electric field, IMF clock angle, dipole tilt angle, and solar-activity index dependent. The Edwards et al. (2020) model underpredicts the maximum current densities throughout, and this is more pronounced for the downwards currents. The mean current densities are also underpredicted, apart from the downwards FACs in the latter half of the interval. This interval of B_y-dominated interplanetary magnetic field and solar wind densities well above nominal are difficult to reproduce by either an MHD or empirical model.

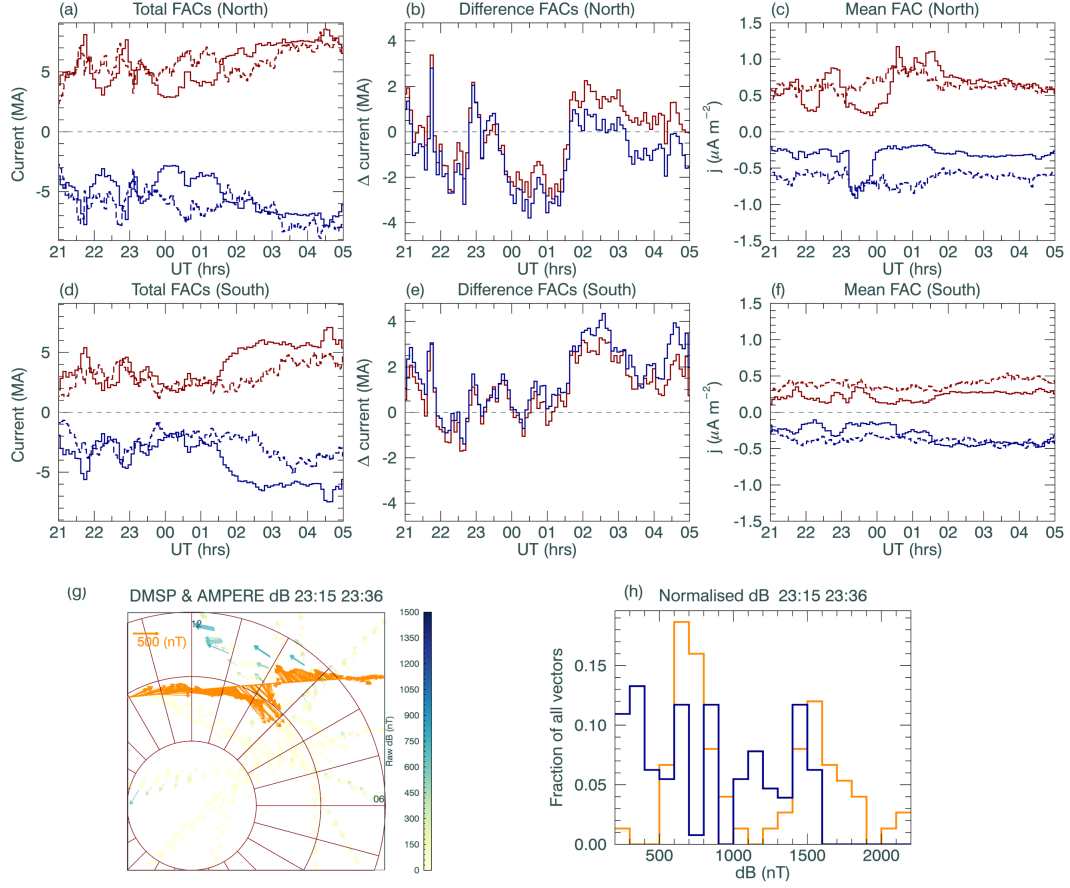


Figure 7. Time series of the magnitudes of the polar cap FACs within 30° co-latitude, for each hemisphere; In (a) and (d) a time series showing the modeled (solid line) and observed (dashed line) FAC magnitudes for North and South respectively, in (b) and (e) the difference between the modeled and observed currents in (a) and (d), and in (c) and (f) we plot the mean current densities. Upwards currents are in red and downwards current are in blue. Panels (a) - (c) for the North, and panels (d) - (f) are for the South. In (g) and (h) we plot a comparison between the perturbed magnetic field data obtained by an example high-latitude DMSP polar cap pass and as obtained for the AMPERE data set; (g) shows a spatial comparison of the satellite tracks for DMSP (orange) and AMPERE (colored vectors) on the dayside polar cap. Red lines mark co-latitudes at 5 degree intervals and MLTs at hour intervals. For clarity, we have only colored the AMPERE vectors. A histogram of vectors from DMSP (orange) and AMPERE (blue) is shown in (h).

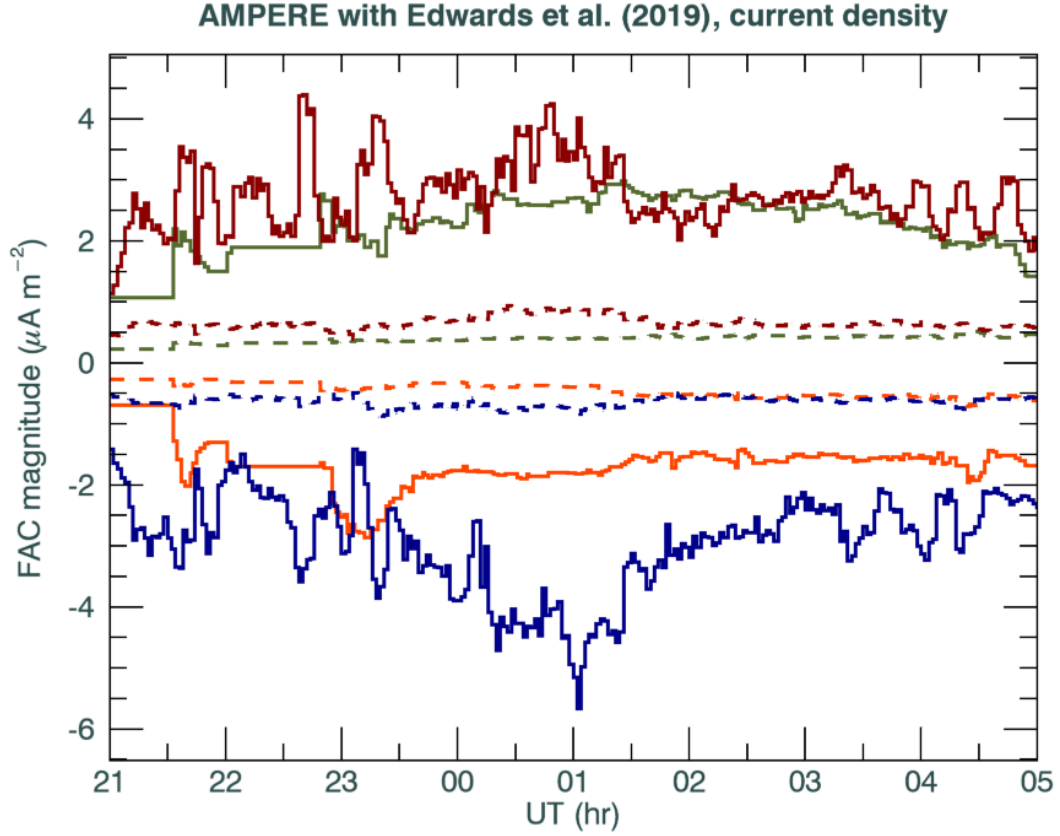


Figure 8. Time series comparing AMPERE maximum and mean current densities with the empirical model of Edwards et al. (2020) for the Northern Hemisphere up to co-latitudes of 30 degrees. Solid or dashed lines show maximum and mean current densities respectively. The AMPERE current densities are shown in red and blue for upwards and downwards FACs, whereas the Edwards et al. (2020) FACs are shown in green and orange respectively.

In Fig. 7 (a) to (f) we have excluded small current densities from our calculations for the observed currents only, however, all modelled currents are considered regardless of magnitude. The AMPERE dataset is constructed from data obtained by situ Iridium® spacecraft that orbit at approximately 780 km altitude. The FACs are calculated from spacecraft measured dB, via a magnetic potential function and spherical harmonic basis function expansion according to Eqn 7.22 of (Waters et al., 2020).

The AMPERE current density maps are given down to a co-latitude of 50 degrees. The advantage of these AMPERE maps is the large scale global coverage that they afford. In contrast, the modeled currents are calculated from the curl of the magnetic field at some distance from the Earth, between 2.5 and 3.0 Earth radii. These currents are then propagated to ionospheric altitudes. Issues with underlying conductivity models or the numerical approximations used in the MHD simulations may be the root cause of the discrepancies in magnitude that we presented here (Gordeev et al., 2015; Ridley et al., 2010). We consider this the most likely scenario given the large numbers of particles that would be precipitating into the polar cap during this time, which we infer from the extremely high solar wind density seen in Fig. 2. The SWMF model of the polar cap incorporates a value for polar cap conductance, but this is set to be equal for both hemispheres, and does not vary with incoming solar wind density. Therefore, larger discrepancies between observed and modeled values should be expected under conditions such as in this interval whereby the incoming solar wind densities are particularly high.

During the interval of interest, the IMF rotates briefly southward at around 21:30 UT, before quickly returning to northward IMF. This is likely associated with the initial shock front of the magnetic cloud associated with an ICME. This is seen in the sharp transitions in the B_z component (green) and the complimentary turning of the B_y (pink) component in panel (a) of Fig. 2. The MHD simulations suggest that the location of reconnection changes rapidly from a low-latitude subsolar location to a high-latitude lobe location over a short period which we present in Fig. 4. Near-contemporaneous activity at main auroral oval latitudes is suggested by the decrease in the AL index in the panel (c) of Fig. 2, which we presume is provoked by a small substorm under the short southward turning of the IMF. The system quickly recovers under northward IMF to stable and quiet auroral-zone activity. Increased activity in the AL index is shown after a period of enhanced solar wind pressure, as shown in panel (b), driven purely by high levels of solar wind density, which we previously assigned to a tail reconnection during IMF-northward nonsubstorm or TRINNI event (Grocott et al., 2003, 2004), as described in Carter et al. (2020). Yu and Ridley (2009) simulated an event whereby the solar wind density increased suddenly from 5 cm^{-3} to 20 cm^{-3} whereas other IMF and solar wind conditions were kept the same and they set the IMF B_y component to 0 nT. They showed a sudden increase in the cross-polar cap potential when the density pulse hit the day-side magnetosphere. They also postulate that the cross-polar cap potential behaviour under this high pressure gradient will result in current systems reminiscent of a two-cell shape, rather than the NBZ configuration more commonly associated with northward IMF. However, we only observe a small increase in the SuperDARN measured cross-polar cap potential during the case presented here, even though the solar density was shown to more than double at the start of the interval, see Fig. 2 (g), and this small increase occurred before the arrival of the pressure pulse. The AMPERE and SSUSI observations are at lower temporal resolution to the Yu and Ridley (2009) MHD simulations, however, it is clear that the NBZ FACs cells dominate throughout this whole interval. The MHD simulations in this paper were run seeded with OMNI data contemporaneous to our observations including the large IMF B_y component, and produced large NBZ cells inside the polar cap.

We tested whether using a alternative and fixed ionospheric conductance value used in the MHD simulation would result in a better correlation between the observations and simulations, both spatially and in FAC magnitude. To do this we ran an additional MHD

simulation with the same numerical model and spatial resolution, at 1-minute time resolution, and with Pedersen and Hall height-integrated conductances at the ionosphere set to values representative of those derived from the SSUSI data set. We took conductance values derived from the SSUSI pass on 16 June 2012 from 22:00 UT to 22:24, from a high-latitude fan shape defined by the region 10 hr to 14 hr MLT and with co-latitudes less than 12 degrees. From these we obtained mean Pedersen and Hall conductance values of 11.97 mho and 16.63 mho respectively. We plot the results below in Fig. 9. Again, as compared to Fig. 7, the simulated total current is underestimated at around 00 UT for the north (a), and now there is a systematic overestimation of total current in the south (c). The discrepancies are larger than with the previous simulation in the latter part of the interval from 02 UT to 05 UT. Spatially, in the bottom row of Fig. 9 and in comparison with Fig. 5, we see little difference in the peak of the MHD-simulated FAC distributions at 22:02 UT, although the magnitudes have increased as indicated by the additional contours and the increased spread to lower latitudes. The peak in the new MHD simulation has shifted poleward at 01:00 UT.

5 Conclusions

We have run an MHD simulation for an interval of interest during the impact of an ICME at the Earth for which we have a wealth of observational evidence. The spatial distributions of predicted field aligned currents in the high-latitude polar cap are in broad agreement with the observations in the Northern Hemisphere. This agreement holds under changing IMF B_Y conditions, whereby both the simulated and observed FACs move many MLT sectors towards dusk. The peak current density locations of the simulated and observed FACs are found to be close in azimuth, although they are less well co-located in terms of latitude. The absolute magnitudes of the modeled currents are at times considerably different to the observed values. The largest differences occur during large solar wind density and a brief change in the orientation of the IMF so that the B_Y component is negative, before returning to positive approximately 1.5 hr later. The interval of interest occurred during Northern Hemisphere summer, when conductances in this hemisphere due to photoionisation will be at their maximum, compared to at a minimum in the Southern Hemisphere. The modeled currents vary spatially to the observed currents in the Southern Hemisphere. Current magnitudes are much lower in the Southern Hemisphere. The underlying conductance model and absence of modifications under varying solar wind density conditions leading to increased particle precipitation in the simulations are likely the major reasons for the discrepancy in the current magnitudes. Uncertainties introduced by the AMPERE fitting technique will be more significant in regions of smaller FAC, but less significant for regions of large current densities such as those presented in this paper, which we have demonstrated through a comparison with measurements made by a different spacecraft. This work highlights the difficulties in comparing observed and modelled currents under extreme solar wind and interplanetary magnetic field conditions, and the need for these comparisons at higher time and spatial resolution, which we leave for future work.

We also observe a rapid change in the implied location of the magnetic reconnection in the model results which moves from the low-latitude equatorial magnetopause in the subsolar region, to a high-latitude lobe region. This occurs within a 15 minute period during a sharp transition from south to northward IMF, which is associated with the shock front of a magnetic cloud that precedes the arrival of an ICME.

The Solar wind Magnetosphere Ionosphere Link Explorer (SMILE) is a joint satellite mission by the European Space Agency and Chinese Academy of Sciences, due for launch in late 2024 (Branduardi-Raymont et al., 2018; Raab et al., 2016). The work in this paper is relevant to the preparations for SMILE. The SMILE spacecraft will operate from a highly inclined, highly elliptical orbit, and will provide an unprecedented view of the magnetosheath and dynamic magnetopause, whilst simultaneously observing the response

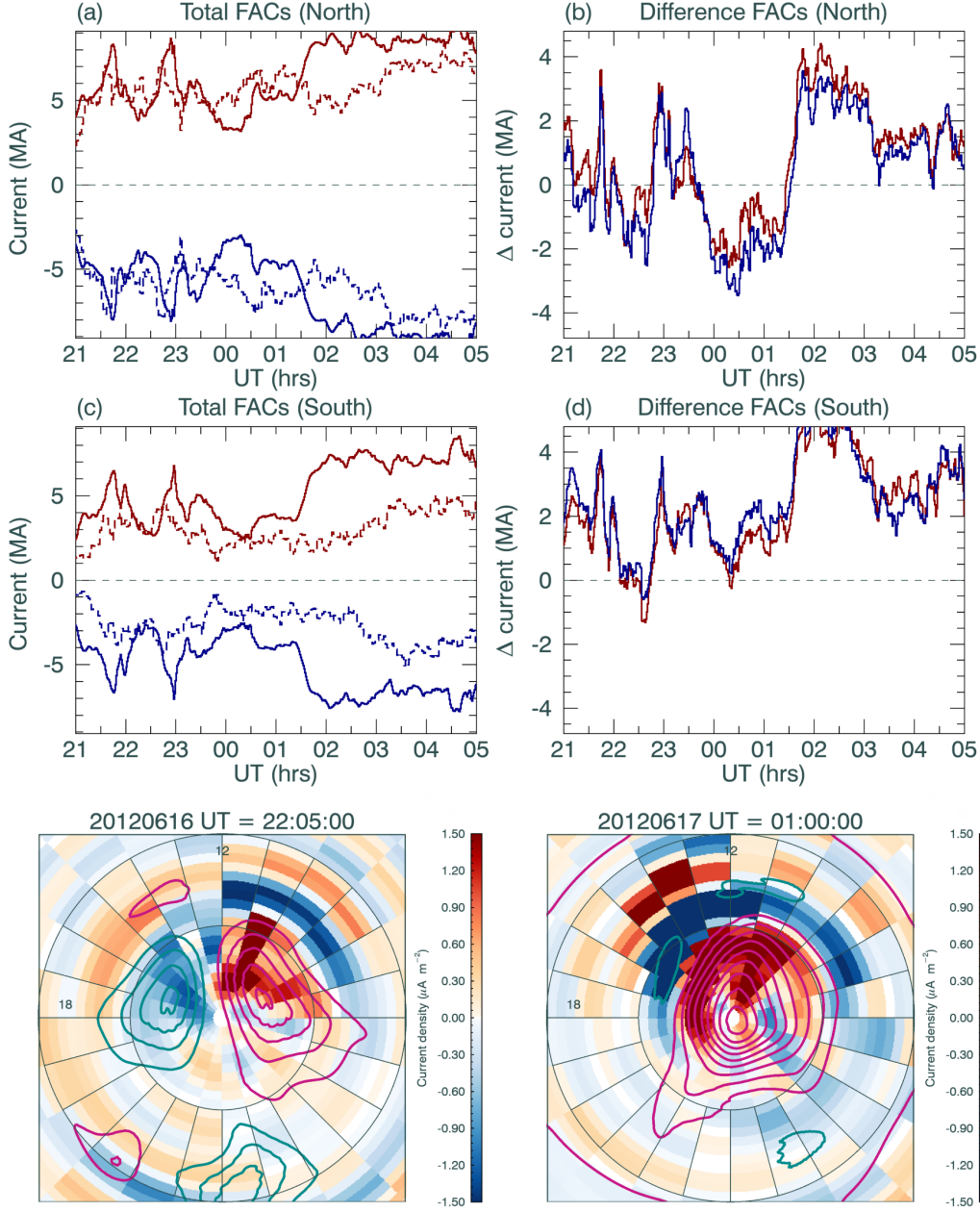


Figure 9. Magnitudes and distributions of FACs from an additional MHD simulation, run with adjusted height-integrated ionospheric conductances, in comparison with the AMPERE-derived values. Panels (a) to (d) are in the same format as Fig. 7, showing the total current within 30° co-latitude for each hemisphere in (a) and (c), and the difference between MHD to AMPERE total current in (b) and (d). The bottom row shows images of Northern Hemisphere AMPERE FACs, with contours of the MHD modeled FACs at two sampled times, in the same format as the AMPERE panels of Fig. 5.

of the ionosphere. The dayside magnetopause will be imaged using the Soft X-ray Imager (SXI). The science goals of SMILE include observing the magnetosphere response under varying solar wind and IMF conditions and SMILE's primary science goals are to consider dayside driving conditions under southward IMF, although on average the incoming IMF will be northwards for half the time. To obtain a truly global and multi-scale picture of the magnetosphere, SMILE must combine its findings with the context provided by other experiments, both ground and space-based, such as with the datasets presented in this paper. Considerable efforts are underway to engage and support the SMILE mission by the global solar-terrestrial physics community, including the authors of this paper. The work in this paper contributes to efforts to model and understand SMILE observations under northward IMF as a part of a set of ongoing simulations. We will detail how these observations compare with the identification of the reconnection site as determined by the SMILE SXI simulator in a subsequent paper.

Acknowledgments

JAC and SEM gratefully acknowledge support from the Science Technology Facilities Council (STFC) consolidated grant ST/N000429/1. JAC also acknowledges support from the L'Oréal-UNESCO For Women In Science UK and Ireland Rising Talents award 2020. The authors wish to thank Thom Edwards for help when using his software and model. AAS and GBR acknowledge support from the UK Space Agency under grant ST/T002964/1. The DMSP/SSUSI file type EDR-AUR data were obtained from <http://ssusi.jhuapl.edu> (data version 0106, software version 7.0.0, calibration period version E0018). AMPERE data were obtained from <http://ampere.jhuapl.edu>. Solar wind data were obtained from the NASA/GSFC OMNI facility (<http://omniweb.gsfc.nasa.gov>), and included the geomagnetic and auroral indices Dst, AU, and AL as provided by the WDC for Geomagnetism, Kyoto (<http://wdc.kugi.kyoto-u.ac.jp/wdc/Sec3.html>). Python libraries were used for field-line tracing, and can be found at <https://pypi.org/project/aacgmv2/> and <https://pypi.org/project/PyGeo>. The authors acknowledge the use of SuperDARN data. SuperDARN is a collection of radars funded by national scientific funding agencies of Australia, Canada, China, France, Japan, South Africa, United Kingdom and United States of America. SuperDARN dates can be found at a number of sites including <https://superdarn.ca/>. This research used the ALICE and SPECTRE High Performance Computing Facility at the University of Leicester. Simulation results have been provided by the Community Coordinated Modeling Center at Goddard Space Flight Center through their public Runs on Request system (<http://ccmc.gsfc.nasa.gov>). The simulations used in this work are archived under the identifier Andrey_Samsonov_032320_1. This work was carried out using the SWMF and BATS-R-US tools developed at the University of Michigan's Center for Space Environment Modeling (CSEM). The modeling tools described in this publication are available online through the University of Michigan for download and are available for use at the Community Coordinated Modeling Center (CCMC).

References

- Anderson, B. J., Takahashi, K., & Toth, B. A. (2000). Sensing global Birkeland currents with iridium® engineering magnetometer data. *Geophys. Res. Letter.*, 27, 4045-4048. doi: 10.1029/2000GL000094
- Branduardi-Raymont, G., Wang, C., Escoubet, C. P., Adamovic, M., Agnolon, D., Berthomier, M., ... Zhu, Z. (2018). SMILE definition study report, European Space Agency, ESA/SCI. In *Smile definition study report* (p. 1-86). doi: <https://doi.org/10.5270/esa.smile.definition.study.report-2018-12>
- Carter, J. A., Milan, S. E., Fogg, A. R., Sangha, H., Lester, M., Paxton, L. J., & Anderson, B. J. (2020). The evolution of long-duration cusp spot emission during lobe reconnection with respect to field-aligned currents. *Journal of Geophysical Research: Space Physics*, 125(7), e2020JA027922. Re-

- trieved from <https://agupubs.onlinelibrary.wiley.com/doi/abs/10.1029/2020JA027922> (e2020JA027922 10.1029/2020JA027922) doi: <https://doi.org/10.1029/2020JA027922>
- Chisham, G., Lester, M., Milan, S. E., Freeman, M. P., Bristow, W. A., Grocott, A., ... Walker, A. D. M. (2007, January). A decade of the Super Dual Auroral Radar Network (SuperDARN): scientific achievements, new techniques and future directions. *Surveys in Geophysics*, 28, 33-109. doi: 10.1007/s10712-007-9017-8
- Cowley, S. W. H., & Lockwood, M. (1992, February). Excitation and decay of solar wind-driven flows in the magnetosphere-ionosphere system. *Annales Geophysicae*, 10, 103-115.
- Coxon, J., Milan, S., Clausen, L., Anderson, B., & Korth, H. (2014). A superposed epoch analysis of the regions 1 and 2 birkeland currents observed by ampere during substorms. *Journal of Geophysical Research: Space Physics*.
- Dungey, J. W. (1963). Interactions of solar plasma with the geomagnetic field. *Planetary and Space Science*, 10, 233-237. doi: 10.1016/0032-0633(63)90020-5
- Edwards, T. R., Weimer, D. R., Olsen, N., Lhr, H., Tobiska, W. K., & Anderson, B. J. (2020). A third generation field-aligned current model. *Journal of Geophysical Research: Space Physics*, 125(1), e2019JA027249. Retrieved from <https://agupubs.onlinelibrary.wiley.com/doi/abs/10.1029/2019JA027249> (e2019JA027249 10.1029/2019JA027249) doi: <https://doi.org/10.1029/2019JA027249>
- Fear, R. C. (2021). The northward imf magnetosphere. In *Magnetospheres in the solar system* (p. 293-309). American Geophysical Union (AGU). Retrieved from <https://agupubs.onlinelibrary.wiley.com/doi/abs/10.1002/9781119815624.ch19> doi: <https://doi.org/10.1002/9781119815624.ch19>
- Fok, M.-C., Buzulukova, N. Y., Chen, S.-H., Gloer, A., Nagai, T., Valek, P., & Perez, J. D. (2014). The comprehensive inner magnetosphere-ionosphere model. *Journal of Geophysical Research: Space Physics*, 119(9), 7522-7540. Retrieved from <https://agupubs.onlinelibrary.wiley.com/doi/abs/10.1002/2014JA020239> doi: <https://doi.org/10.1002/2014JA020239>
- Gordeev, E., Sergeev, V., Honkonen, I., Kuznetsova, M., Rasttter, L., Palmroth, M., ... Wiltberger, M. (2015). Assessing the performance of community-available global mhd models using key system parameters and empirical relationships. *Space Weather*, 13(12), 868-884. Retrieved from <https://agupubs.onlinelibrary.wiley.com/doi/abs/10.1002/2015SW001307> doi: <https://doi.org/10.1002/2015SW001307>
- Grocott, A., Badman, S., Cowley, S., Yeoman, T., & Cripps, P. (2004, May). The influence of IMF By on the nature of the nightside high-latitude ionospheric flow during intervals of positive IMF Bz. *Annales Geophysicae*, 22, 1755-1764. doi: 10.5194/angeo-22-1755-2004
- Grocott, A., Cowley, S. W. H., & Sigwarth, J. B. (2003, February). Ionospheric flow during extended intervals of northward but B_y-dominated IMF. *Annales Geophysicae*, 21, 509-538. doi: 10.5194/angeo-21-509-2003
- Heppner, J. P., & Maynard, N. C. (1987). Empirical high-latitude electric field models. *Journal of Geophysical Research: Space Physics*, 92(A5), 4467-4489. Retrieved from <https://agupubs.onlinelibrary.wiley.com/doi/abs/10.1029/JA092iA05p04467> doi: <https://doi.org/10.1029/JA092iA05p04467>
- King, J. H., & Papitashvili, N. E. (2005, February). Solar wind spatial scales in and comparisons of hourly Wind and ACE plasma and magnetic field data. *Journal of Geophysical Research (Space Physics)*, 110, 2104. doi: 10.1029/2004JA010649
- Lu, G., Li, W. H., Raeder, J., Deng, Y., Rich, F., Ober, D., ... Newell, P. (2011). Reversed two-cell convection in the northern and southern hemispheres during northward interplanetary magnetic field. *Journal of Geo-*

- physical Research: Space Physics, 116(A12). Retrieved from <https://agupubs.onlinelibrary.wiley.com/doi/abs/10.1029/2011JA017043> doi: <https://doi.org/10.1029/2011JA017043>
- Milan, S. E., Clausen, L. B. N., Coxon, J. C., Carter, J. A., Walach, M.-T., Laundal, K., ... Anderson, B. J. (2017, March). Overview of Solar Wind-Magnetosphere-Ionosphere-Atmosphere Coupling and the Generation of Magnetospheric Currents. *Space Science Reviews*, 206, 547-573. doi: 10.1007/s11214-017-0333-0
- Paxton, L. J., Meng, C.-I., Fountain, G. H., Ogorzalek, B. S., Darlington, E. H., Gary, S. A., ... Linstrom, L. A. (1992, June). Special Sensor Ultraviolet Spectrographic Imager (SSUSI) - an instrument description. In S. Chakrabarti & A. B. Christensen (Eds.), *Instrumentation for planetary and terrestrial atmospheric remote sensing* (Vol. 1745, p. 2-15). doi: 10.1117/12.60595
- Paxton, L. J., & Zhang, Y. (2016). *Far ultraviolet imaging of the aurora. In Space Weather Fundamentals*. CRC press.
- Raab, W., Branduardi-Raymont, G., Wang, C., Dai, L., Donovan, E., Enno, G., ... Zheng, J. (2016). SMILE: a joint ESA/CAS mission to investigate the interaction between the solar wind and Earth's magnetosphere. In J.-W. A. den Herder, T. Takahashi, & M. Bautz (Eds.), *Space telescopes and instrumentation 2016: Ultraviolet to gamma ray* (Vol. 9905, pp. 1 - 9). SPIE. Retrieved from <https://doi.org/10.1117/12.2231984> doi: 10.1117/12.2231984
- Ridley, A., Gombosi, T., & Dezeew, D. (2004, Feb). Ionospheric control of the magnetosphere: conductance. *Annales Geophysicae*, 22(2), 567-584. doi: 10.5194/angeo-22-567-2004
- Ridley, A. J., De Zeeuw, D. L., & Rasttler, L. (2016). Rating global magnetosphere model simulations through statistical data-model comparisons. *Space Weather*, 14(10), 819-834. Retrieved from <https://agupubs.onlinelibrary.wiley.com/doi/abs/10.1002/2016SW001465> doi: <https://doi.org/10.1002/2016SW001465>
- Ridley, A. J., Gombosi, T. I., Sokolov, I. V., Tóth, G., & Welling, D. T. (2010). Numerical considerations in simulating the global magnetosphere. *Annales Geophysicae*, 28(8), 1589-1614. Retrieved from <https://angeo.copernicus.org/articles/28/1589/2010/> doi: 10.5194/angeo-28-1589-2010
- Samsonov, A. A., Sibeck, D. G., & Yu, Y. (2010). Transient changes in magnetospheric-ionospheric currents caused by the passage of an interplanetary shock: Northward interplanetary magnetic field case. *Journal of Geophysical Research: Space Physics*, 115(A5). Retrieved from <https://agupubs.onlinelibrary.wiley.com/doi/abs/10.1029/2009JA014751> doi: <https://doi.org/10.1029/2009JA014751>
- Sandholt, P. E., Farrugia, C. J., Moen, J., Noraberg, O., Lybekk, B., Sten, T., & Hansen, T. (1998). A classification of dayside auroral forms and activities as a function of interplanetary magnetic field orientation. *Journal of Geophysical Research: Space Physics*, 103(A10), 23325-23345. Retrieved from <http://dx.doi.org/10.1029/98JA02156> doi: 10.1029/98JA02156
- Shue, J.-H., & Song, P. (2002, April). The location and shape of the magnetopause. *Planetary and Space Science*, 50, 549-558. doi: 10.1016/S0032-0633(02)00034-X
- Shue, J.-H., Song, P., Russell, C. T., Steinberg, J. T., Chao, J. K., Zastenker, G., ... Kawano, H. (1998, August). Magnetopause location under extreme solar wind conditions. *Journal of Geophysical Research*, 103, 17691-17700. doi: 10.1029/98JA01103
- Siscoe, G. L., Crooker, N. U., Erickson, G. M., Sonnerup, B. U. Ö., Siebert, K. D., Weimer, D. R., ... Maynard, N. C. (2000, January). Global Geometry of Magnetospheric Currents Inferred From MHD Simulations. *Washington DC American Geophysical Union Geophysical Monograph Series*, 118, 41. doi:

- 10.1029/GM118p0041
- Tth, G., Sokolov, I. V., Gombosi, T. I., Chesney, D. R., Clauer, C. R., De Zeeuw, D. L., ... Kta, J. (2005). Space weather modeling framework: A new tool for the space science community. *Journal of Geophysical Research: Space Physics*, 110(A12). Retrieved from <https://agupubs.onlinelibrary.wiley.com/doi/abs/10.1029/2005JA011126> doi: <https://doi.org/10.1029/2005JA011126>
- Waters, C. L., Anderson, B. J., Green, D. L., Korth, H., Barnes, R. J., & Vanhamaki, H. (2020). Science data products for AMPERE. In *Ionospheric multi-spacecraft analysis tools*, eds: Dunlop, m., luhr, h., p141-165, springer nature, switzerland (p. 141-165). doi: 10.1007/978-3-030-26732-2
- Waters, C. L., Anderson, B. J., & Liou, K. (2001). Estimation of global field aligned currents using the iridium® system magnetometer data. *Geophys. Res. Letter.*, 28, 2165-2168. doi: 10.1029/2000GL012725
- Yu, Y., & Ridley, A. J. (2009). The response of the magnetosphere-ionosphere system to a sudden dynamic pressure enhancement under southward imf conditions. *Annales Geophysicae*, 27(12), 4391-4407. Retrieved from <https://angeo.copernicus.org/articles/27/4391/2009/> doi: 10.5194/angeo-27-4391-2009